New modal wave-front sensor: application to adaptive confocal fluorescence microscopy and two-photon excitation fluorescence microscopy

Martin J. Booth, Mark A. A. Neil, and Tony Wilson

Department of Engineering Science, University of Oxford, Parks Road, Oxford OX1 3PJ, UK

Received June 18, 2001; revised manuscript received March 28, 2002; accepted May 30, 2002

Confocal and multiphoton microscopes are particularly sensitive to specimen- or system-induced aberrations, which result in decreased resolution and signal-to-noise ratio. The inclusion of an adaptive optics correction system could help overcome this limitation and restore diffraction-limited performance, but such a system requires a suitable method of wave-front measurement. By extending the concept of a modal wave-front sensor previously described by Neil *et al.* [J. Opt. Soc. Am. A **17**, 1098–1107 (2000)], we present a new sensor capable of measuring directly the Zernike aberration modes introduced by a specimen. This modal sensor is particularly suited to applications in three-dimensional microscopy because of its inherent axial selectivity; only those wave fronts originating in the focal region contribute to the measured signal. Four wave-front sensor configurations are presented and their input response is characterized. Sensitivity matrices and axial responses are presented.

OCIS codes: 010.1080, 010.7350, 170.1790, 180.3520.

1. INTRODUCTION

A confocal microscope permits three-dimensional imaging of volume objects by the inclusion of a pinhole in the detector path, which eliminates out-of-focus light.[1,2] Multiphoton microscopy exhibits similar three-dimensional imaging properties without the use of a detector pinhole owing to the confinement of fluorescence emission to the focal region.[3] Both methods are, however, very sensitive to aberrations induced by the specimen or the optical system[4] and could therefore benefit from an adaptive optics approach.[5,6] We have previously discussed the design and implementation of a modal wave-front sensor (WFS) that can measure the amount of each Zernike aberration component within an aberrated input wave front.[7,8,9] The sensor shows a linear response for small aberrations and is therefore ideally suited to incorporation into a closed-loop adaptive system. The WFS was found to be particularly useful in situations where the aberration consisted mainly of a low number of Zernike modes. It has also been shown that such low-order aberrations predominate in confocal and multiphoton microscopy.[4]

In this paper we briefly review the previously introduced WFS and then show how the concept can be extended to allow incorporation into confocal and two-photon microscope systems. Three WFS configurations are presented for the confocal system and one for the two-photon system. Expressions describing the response of each WFS configuration are derived by using a scalar theory, and response curves for several low-order aberration modes are presented. We use modal sensitivity matrices to characterize the sensor in each microscope configuration and show that the properties of the matrices are similar to those derived for the simple WFS of the previous paper.[7] By considering the response of the WFS to a defocused fluorescent plane object, we show that the sensor demonstrates axial selectivity in a manner similar to the case of the confocal microscope and therefore responds only to wave fronts emanating from the focal region. This is an intrinsic advantage over conventional methods, such as Shack–Hartmann sensors or interferometers, which could be swamped by out-of-focus fluorescence.

2. WAVE-FRONT SENSING IN A CONFOCAL FLUORESCENCE MICROSCOPE

In a previous paper[7] we described conceptually a WFS in which an aberrated input beam was split into two so that each beam consisted of identical aberrated wave fronts. The first beam then passed through a phase plate that added an amount of a chosen aberration mode to the input wave front. The second path passed through a phase plate that effectively subtracted the same amount of the chosen aberration from the input wave front. We refer to this process as wave-front biasing. The biased beams were then focused onto separate detector pinholes that sample the central region of each focal spot. When the input wave front is unaberrated, the aberrations introduced in the two paths are equal in magnitude and cause equal distortion of the focal spot and hence equal detector signals. However, if the input and bias aberration modes are identical, then the process of biasing will cause one wave front to become partially flattened, and the corresponding focal spot will become brighter. In the other path, the biasing will increase the magnitude of the aberration and result in a dimmer focal spot. The output signal was taken as the difference between the two detector signals and was found to be proportional to the amplitude of the input aberration. Multiple sensors can be built to

1084-7529/2002/102112-09$15.00

measure each aberration mode of interest. It was shown that Zernike polynomials are a useful basis as aberration modes. In the limit of small bias magnitude and small detector pinhole, the Zernike-based sensor responded exclusively to its design mode. For larger values of bias and pinhole size, it was shown that only certain limited cross sensitivity existed between modes.

We now describe how the WFS concept can be extended for implementation in adaptive aberration-correction systems for confocal fluorescence microscopes and two-photon excitation fluorescence microscopes. Figure 1 shows a schematic of a confocal microscope setup including an aberrating specimen. In this microscope, illumination light from a laser passes through the microscope optics and part of the specimen before reaching the focal plane. Fluorescence emission from the focal region passes back through the specimen and the microscope optics, is then separated by a beam splitter, and is focused onto the pinhole detector. Fluorescence light emitted in parts of the illumination cone outside the focal plane does not pass through the pinhole and is not detected. Any aberrations introduced by the specimen are induced in both the illumination path and the emission path. We can model the effects of such a specimen by replacing it with an aberration-free specimen and by placing an equivalent phase plate in the Fourier plane of the objective such that it lies in both the illumination and the emission paths (i.e., plane II in Fig. 1). From the nature of the induced aberrations it is also apparent that an adaptive confocal microscope requires aberration correction in both paths. The aberration-correction element, such as a deformable mirror, should therefore also be situated in plane II. This double-pass nature of the confocal microscope offers several wave-front-biasing possibilities. For example, in addition to providing aberration correction, and adaptive element situated in plane II could also apply the bias aberrations to the illumination and the emission wave fronts simultaneously. Alternatively, the wave-front biasing could be performed by different elements placed elsewhere in the microscope: Biasing elements can be included in the Fourier planes of either the illumination path (plane I) or the emission path (plane III) or in both paths (plane II). Schematic representations of each configuration are shown in Figs. 2A–2C. For clarity, the diagrams are drawn "unfolded" with two separate objective lenses situated on either side of the focal plane; typically, however, the same objective lens would be used for illumination and collection. In each case, the input aberration as introduced by the specimen is represented by the phase function $aZ_k(r, \theta)$, where $Z_k(r, \theta)$ is a Zernike polynomial, whose arguments r and θ are the polar coordinates in the Fourier plane, and a is its amplitude. Similarly, the bias aberration is represented by $bZ_i(r, \theta)$, where $Z_i(r, \theta)$ is generally a different Zernike polynomial with amplitude b. The Zernike polynomials are described in Appendix A.

In the model used for this analysis, the illumination from a point source passes through the illumination-path phase plates and is then focused by the objective lens to create an aberrated spot in the fluorescent specimen. The emitted light is collected by another lens and passes through the emission-path phase plates before being focused onto the detector pinhole. In the real microscope, since the same objective lens is used to both illuminate the specimen and collect the emitted light, the aberrations introduced in the illumination path are the spatial inversions of those encountered by the emitted light. We therefore find it useful to define the $\sim$ operator as

$$\tilde{g}(r, \theta) = g(r, \theta + \pi). \tag{1}$$

Figure 2D shows a configuration that is useful in a two-photon excitation fluorescence microscope. Often, owing to their inherent sectioning ability, these microscopes are used without a detector pinhole. In this configuration, any aberrations introduced in the emission path have no effect on the detected signal, so they have been neglected. For the same reason, biasing occurs only on the illumination path. We note that configurations A, B, and C would all be suitable for use in two-photon excitation micro-

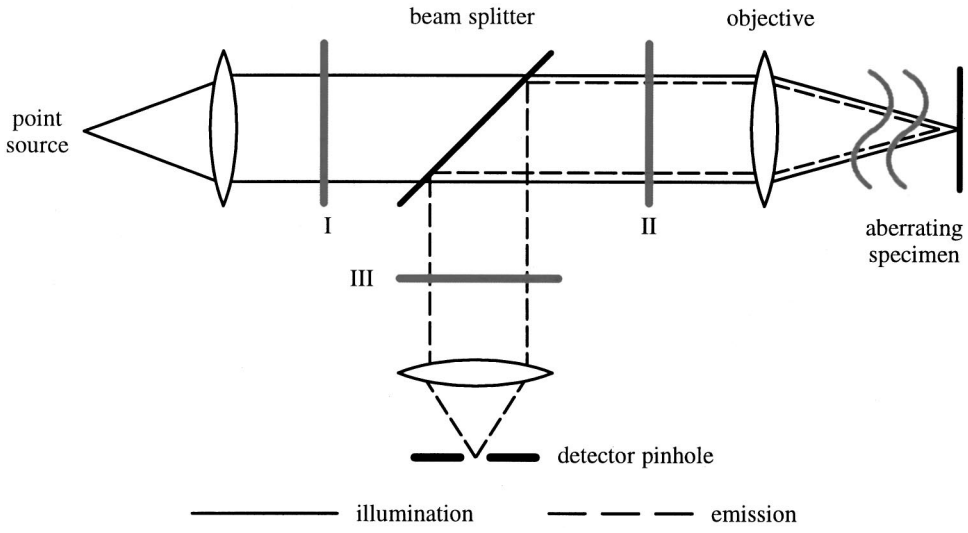

Fig. 1. Schematic diagram of a confocal microscope with an aberrating specimen. Planes I, II and III are all conjugate to the pupil of the objective lens (the matching optics have been omitted for clarity) and represent possible locations of biasing and correction elements. The specimen-induced aberrations can be modeled by an equivalent phase plate situated in plane II.

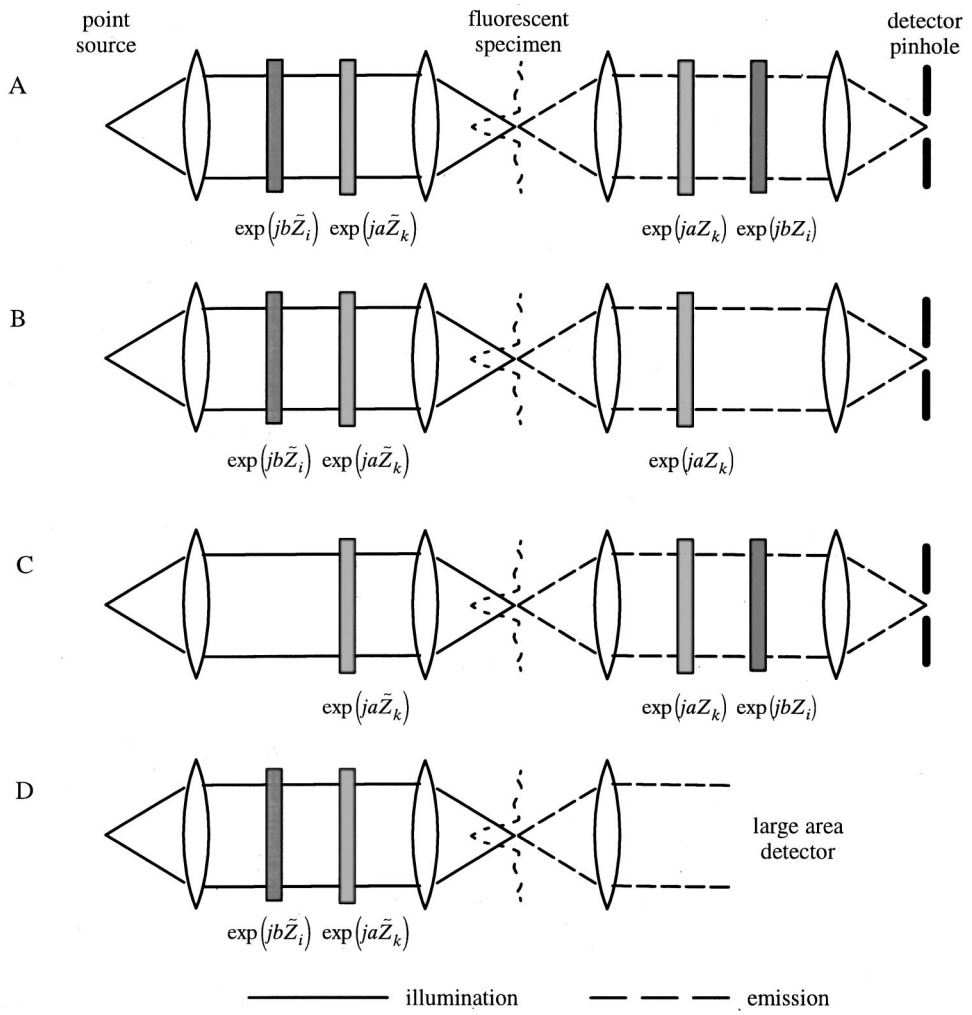

Fig. 2. Schematic descriptions of different confocal wave-front sensor biasing configurations where biasing occurs in A, illumination and emission path; B, illumination path only; C, emission path only. Configuration D, suitable for two-photon microscopy, uses illumination-path biasing and a large-area detector.

scopes that incorporate a detector pinhole, although we do not present results of this here.

In each case we calculate a function $f(\nu, \xi)$ that describes the fluorescence distribution in the focal region in terms of the radial coordinate ν and the azimuthal coordinate ξ. For single-photon fluorescence this is formally identical to the intensity point-spread function (PSF) and is given by the modulus squared of the Fourier transform (FT) of the effective pupil function $P^f(r, \theta)$ of the objective:

$$f(\nu, \xi) = |\mathcal{F}[P^f(r, \theta)]|^2, \tag{2}$$

where $\mathcal{F}$ denotes the FT.[10] This is a useful formulation since the effective pupil function can incorporate any aberrations introduced into the system. In a similar manner, we may also derive the intensity PSF $h(\nu, \xi)$ of the optics that image the fluorescent spot onto the detector plane in terms of the pupil function $P^h(r, \theta)$ of the objective in the emission path:

$$h(\nu, \xi) = |\mathcal{F}[P^h(r, \theta)]|^2. \tag{3}$$

Here we have implicitly made the approximation that the excitation and emission wavelengths are the same. Each aberration-mode measurement is taken as the difference between the detector signal with the positive-bias aberration applied and the signal with the negative-bias aberration applied. We therefore introduce the subscripts 1 and 2 for the positive and negatively biased cases, respectively. The intensity distribution at the detector pinhole is given by the spatial convolution of the fluorescence distribution, f_1 or f_2, and the intensity PSF, h_1 or h_2, respectively. Integration of this intensity over the detector pinhole gives the power incident on that detector as

$$W_{1,2} = \int_0^{2\pi} \int_0^{\nu_p} (f_{1,2} * h_{1,2}) \nu \mathrm{d}\nu \mathrm{d}\xi, \tag{4}$$

where ν_p is the pinhole radius and the symbol $*$ denotes the convolution operator, which is defined in Appendix B. If we take the output signal to be the difference between the detector signals for positive and negative bias, we find the output to be

$$\Delta W_{ik} = W_1 - W_2 = \int_0^{2\pi} \int_0^{\nu_p} [(f_1 * h_1) - (f_2 * h_2)] \nu \mathrm{d}\nu \mathrm{d}\xi. \tag{5}$$

The subscripts i and k represent the index of the bias and input aberrations, respectively. We define the sensitivity of a mode i biased aberration sensor to an input mode k by

$$S_{ik} = -\left.\frac{\partial \Delta W_{ik}}{\partial a}\right|_{a=0} = -\int_0^{2\pi}\int_0^{\nu_p}\frac{\partial}{\partial a}[(f_1 * h_1) - (f_2 * h_2)]_{a=0}\nu \mathrm{d}\nu \mathrm{d}\xi, \quad (6)$$

where again a is the amplitude of the input-aberration mode. A sensitivity matrix $\mathbf{S}$ can be constructed from the elements S_{ik}. This permits us to describe the response of the sensor, in a linear approximation, as

$$\mathbf{w} = \mathbf{S}\mathbf{a}, \quad (7)$$

where $\mathbf{w}$ is the vector whose elements are the sensor output signals of Eq. (5) and $\mathbf{a}$ is the vector containing the input-mode amplitudes.

The infinite integrals and convolutions of the above results do not lend themselves easily to numerical computation. Instead we transform the integrals into Fourier space, where they are expressed in terms of optical transfer functions[10] (OTFs). Using the convolution theorem, we write Eq. (4) in the form

$$W_{1,2} = \int_0^{2\pi}\int_0^{\nu_p}\mathcal{F}^{-1}[F_{1,2}H_{1,2}]\nu \mathrm{d}\nu \mathrm{d}\xi, \quad (8)$$

where $F_{1,2}(r,\ \theta)$ and $H_{1,2}(r,\ \theta)$ are respectively the FTs of $f_{1,2}(\nu,\ \xi)$ and $h_{1,2}(\nu,\ \xi)$, and $\mathcal{F}^{-1}[\ \cdot\ ]$ denotes the inverse FT. $F_{1,2}(r,\ \theta)$ and $H_{1,2}(r,\ \theta)$ are essentially the OTFs of the illumination and the imaging optics, respectively, which can be expressed as autocorrelations of the relevant pupil functions,[10]

$$F_{1,2}(r,\ \theta) = P^f_{1,2}(r,\ \theta) \otimes P^f_{1,2}(r,\ \theta)^*, \quad (9)$$

$$H_{1,2}(r,\ \theta) = P^h_{1,2}(r,\ \theta) \otimes P^h_{1,2}(r,\ \theta)^*, \quad (10)$$

where * denotes the complex conjugate and $\otimes$ is the correlation operator, which is defined in Appendix B. These are finite autocorrelations of functions defined over the unit circle and are equal to zero for $r > 2$. In this particular case, the actual limits of the correlation integrations would be finite owing to the finite extent of the two functions in the correlation operation.

By performing the integrals in ν and ξ we can simplify Eq. (8) further to

$$W_{1,2} = \frac{\nu_p}{2\pi^3}\int_0^{2\pi}\int_0^{2}F_{1,2}H_{1,2}J_1(r\nu_p)\mathrm{d}r\mathrm{d}\theta, \quad (11)$$

where $J_1(\ \cdot\ )$ is the first-order Bessel function of the first kind. A normalization factor has been introduced so that the total power in the detector plane is equal to unity. Since $F_{1,2}$ and $H_{1,2}$ are finite convolutions and the limits of the integration are finite, this formulation is more suitable for numerical integration. Equation (11) can be simplified further by recalling that $F_{1,2}$ and $H_{1,2}$ are OTFs and therefore have the following property:

$$F_{1,2}(r,\ \theta + \pi) = F_{1,2}(r,\ \theta)^*, \quad (12)$$

and similarly for $H_{1,2}$. This property arises from the fact that the real and imaginary parts of the FT of a real function (the intensity PSF in this case) must be even and odd functions, respectively. Also, it is easily shown that the product of two such functions has the same property such that on integration over the circle, the imaginary part of the product $F_{1,2}H_{1,2}$ becomes zero. Moreover, the real part exhibits twofold rotational symmetry; the integration can be performed over a semicircle. The integral can therefore be expressed as

$$W_{1,2} = \frac{\nu_p}{\pi^3}\int_0^{\pi}\int_0^{2}\mathrm{Re}[F_{1,2}H_{1,2}]J_1(r\nu_p)\mathrm{d}r\mathrm{d}\theta. \quad (13)$$

The output difference signal follows as

$$\Delta W_{ik} = \frac{\nu_p}{\pi^3}\int_0^{\pi}\int_0^{2}\{\mathrm{Re}[F_1H_1] - \mathrm{Re}[F_2H_2]\}J_1(r\nu_p)\mathrm{d}r\mathrm{d}\theta \quad (14)$$

and the sensitivity as

$$S_{ik} = -\frac{\nu_p}{\pi^3}\int_0^{\pi}\int_0^{2}\frac{\partial}{\partial a}\{\mathrm{Re}[F_1H_1] - \mathrm{Re}[F_2H_2]\}_{a=0}J_1(r\nu_p)\mathrm{d}r\mathrm{d}\theta. \quad (15)$$

The specific calculations for each configuration are now considered in more detail.

A. Configuration A

We now consider configuration A, in which a bias aberration is introduced into both paths. We take the object to be a fluorescent sheet oriented perpendicularly to the optic axis and displaced a distance u from the focal plane, where u is a normalized axial coordinate and is related to the real coordinate z by[1]

$$u = \frac{\pi D^2 z}{2\lambda L^2} \approx \frac{8\pi}{\lambda}z\sin^2\left(\frac{\alpha}{2}\right), \quad (16)$$

where D and L are the diameter and the focal length of the objective lens, λ is the wavelength, and α is the semiaperture angle. The pupil phase function is given by the sum of the input and bias aberrations and a quadratic defocus term[1] such that

$$P^f_{1,2}(r,\ \theta) = \exp\left(ja\tilde{Z}_k \pm jb\tilde{Z}_i + j\frac{ur^2}{2}\right), \quad (17)$$

$$P^h_{1,2}(r,\ \theta) = \exp\left(jaZ_k \pm jbZ_i + j\frac{ur^2}{2}\right). \quad (18)$$

The subscripts 1 and 2 refer to the positively and negatively biased cases, respectively. The OTFs are readily calculated by substituting from Eqs. (17) and (18) into Eqs. (9) and (10). Hence we find that

$$F_{1,2}(r,\ \theta) = \tilde{H}_{1,2}(r,\ \theta) = H_{1,2}(r,\ \theta)^*. \quad (19)$$

The output signal of Eq. (14) can therefore be written as

$$\Delta W_{ik} = \frac{\nu_p}{\pi^3}\int_0^{\pi}\int_0^{2}[|H_1|^2 - |H_2|^2]J_1(r\nu_p)\mathrm{d}r\mathrm{d}\theta. \quad (20)$$

The equivalent sensitivity of Eq. (15) is found by differentiation of Eq. (20).

B. Configurations B and C

The intensity distribution in the detector plane is given by the convolution of the intensity PSF of the illumination optics and the intensity PSF of the collection optics; this intensity distribution is integrated over the detector pinhole to derive the signals W_1 and W_2. It follows that the output signals obtained in configurations B and C are identical since the illumination and imaging optics are merely interchanged. We therefore consider only configuration C here. The pupil functions are given by

$$P^f_{1,2}(r,\ \theta) = \exp\left(ja\tilde{Z}_k + j\frac{ur^2}{2}\right), \tag{21}$$

$$P^h_{1,2}(r,\ \theta) = \exp\left(jaZ_k \pm jbZ_i + j\frac{ur^2}{2}\right). \tag{22}$$

Again, the OTFs are calculated by using Eqs. (9) and (10). Since the bias aberrations appear only in the emission-path pupil function $P^h(r,\ \theta)$ we can write the excitation-path OTF in both cases as

$$F(r,\ \theta) = F_{1,2}(r,\ \theta). \tag{23}$$

The output signal is therefore

$$\Delta W_{ik} = \frac{\nu_p}{\pi^3}\int_0^{\pi}\int_0^{2} \mathrm{Re}[F(H_1 - H_2)]J_1(r\nu_p)\mathrm{d}r\mathrm{d}\theta, \tag{24}$$

and the sensitivity is found by differentiation of Eq. (24).

C. Configuration D

The intensity of the emitted two-photon fluorescence is proportional to the square of the illumination intensity and hence to the fourth power of the illumination amplitude. This nonlinear response confines the fluorescence emission to the focal region. Two-photon microscopes are therefore normally used without a confocal pinhole in order to maximize signal strength at the expense of only a small decrease in axial sectioning ability.[11] In configuration D we use a large-area detector and no pinhole in the emission path. We neglect any aberrations introduced in that path since they have no effect on the detected signal. Biasing occurs only on the illumination path, and the corresponding PSFs are given by

$$f_{1,2}(\nu,\ \xi) = |\mathcal{F}[P^f_{1,2}(r,\ \theta)]|^4, \tag{25}$$

where the pupil function is

$$P^f_{1,2}(r,\ \theta) = \exp\left(ja\tilde{Z}_k \pm jb\tilde{Z}_i + j\frac{ur^2}{2}\right). \tag{26}$$

The detected intensity is simply the total intensity in the PSF:

$$W_{1,2} = \lim_{\nu_p \to \infty}\int_0^{2\pi}\int_0^{\nu_p} f_{1,2}\nu\mathrm{d}\nu\mathrm{d}\xi. \tag{27}$$

If we transform Eq. (27) into the frequency domain and take the limit as ν_p tends to infinity, we obtain

$$W_{1,2} = \frac{2}{\pi^3 - 16\pi/3}\int_0^{\pi}\int_0^{2}|F_{1,2}|^2 r\mathrm{d}r\mathrm{d}\theta, \tag{28}$$

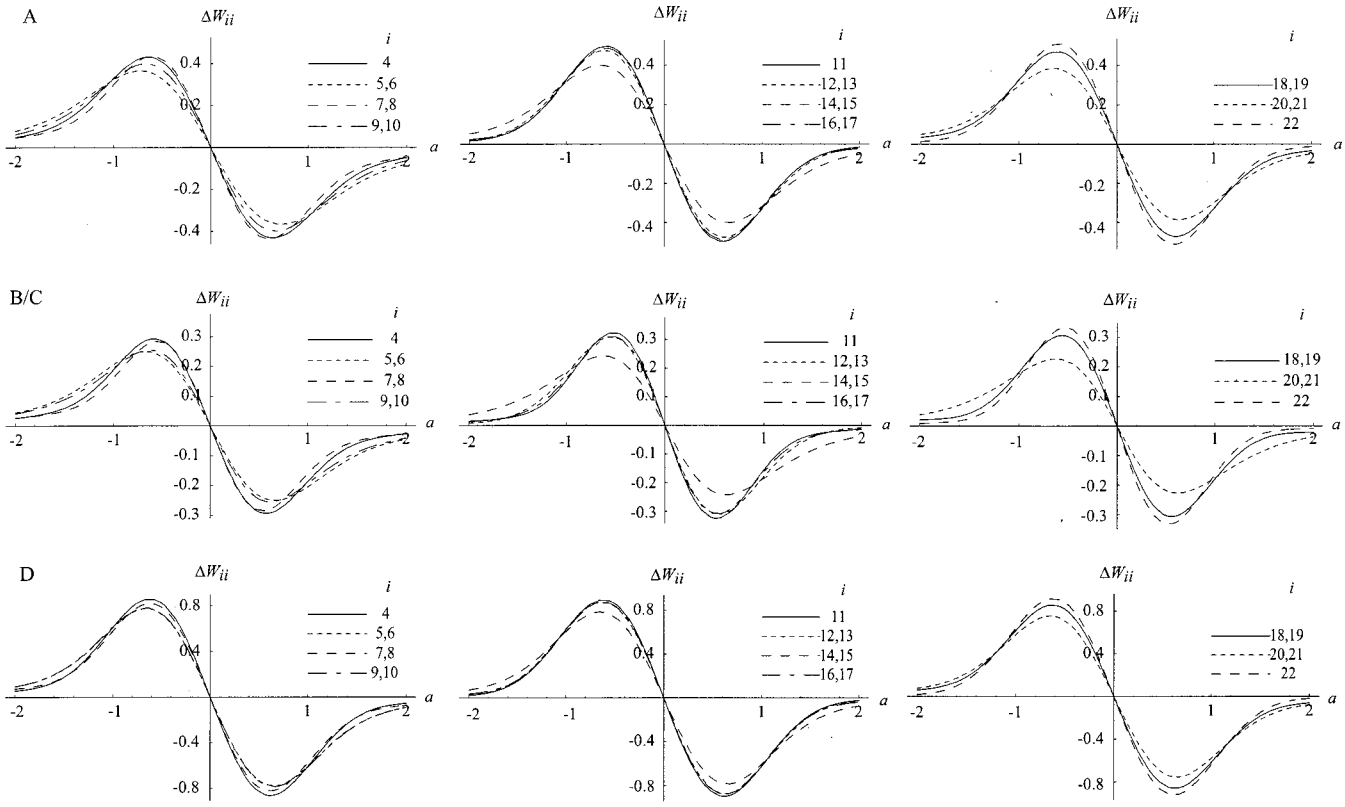

Fig. 3. Output signals for a fluorescent plane object in each wave-front sensor configuration. For configuration A, $\nu_p = \pi$ and $b = 0.5$. For configuration B/C, $\nu_p = \pi$ and $b = 0.5$. For configuration D, $b = 0.55$.

where $F_{1,2}(r, \theta)$ is the equivalent single-photon OTF, given by

$$F_{1,2}(r, \theta) = P^f_{1,2}(r, \theta) \otimes P^f_{1,2}(r, \theta)^*. \tag{29}$$

In Eq. (28), we have introduced a normalization factor to ensure that the total power in the output plane is unity. We also note that the integration is now performed over a semicircle owing to the twofold rotational symmetry of the OTF. The output signal therefore becomes

$$\Delta W_{ik} = \frac{2}{\pi^3 - 16\pi/3} \int_0^{\pi} \int_0^2 [|F_1|^2 - |F_2|^2] r \mathrm{d}r \mathrm{d}\theta, \tag{30}$$

and the sensitivity is again found by differentiation with respect to a.

D. Parameter Choice

For WFS configurations A–C there are two parameters with which one can alter the characteristics of each aberration sensor: the bias b and the pinhole radius ν_p. For configuration D, where there is no pinhole, the bias is the only free parameter. We can use these parameters to optimize the sensor for some property, for example, maximum sensitivity S_{ii}. Generally, this maximum occurs at different combinations of b and ν_p for each different aberration-mode sensor, although the maximum is broad and the optimum values of b and ν_p are similar for the different modes. It is therefore convenient to use an average of these values.

Normally, when using a confocal microscope, one would select the pinhole size to give a balance between signal-to-noise ratio and axial resolution. We therefore choose the value of ν_p to be typical for normal operation of a confocal microscope,[2] namely, $\nu_p = \pi$. We note that the first zero of the Airy disk occurs at $\nu = 1.22\pi$. Using a fluorescent plane as the object, we can calculate the bias b that gives maximum sensitivity. For this pinhole size, the optimum bias is ~0.5 with configuration A and ~0.7 with configuration B/C. In configuration D, where the pinhole has infinite radius, we find an optimum bias of 0.55. These values are used in the following calculations.

E. Response to a Fluorescent Sheet in the Focal Plane

Here we consider the response of each configuration when the object is a fluorescent sheet in the focal plane ($u = 0$). The pinhole size and bias for each case are taken as the values described above. In Fig. 3 we show the difference signals of Eqs. (20), (24), and (30) as functions of the size a of the input aberration calculated for sensors designed to detect Zernike modes from defocus ($i = 4$) to second-order spherical ($i = 22$). We do not include tip and tilt since they are automatically corrected by the double-pass nature of a single-lens confocal microscope. Any tilt introduced on the excitation path, thus laterally displacing the spot, is essentially removed on the emission path. Adjacent modes (e.g., $i = 5$ and $i = 6$) differ only by a $\pi/2$ rotation, so the curves are identical. Each sensor configuration exhibits a linear response in a region around $a = 0$. This is an important property when the sensor is used in a closed-loop correction system.

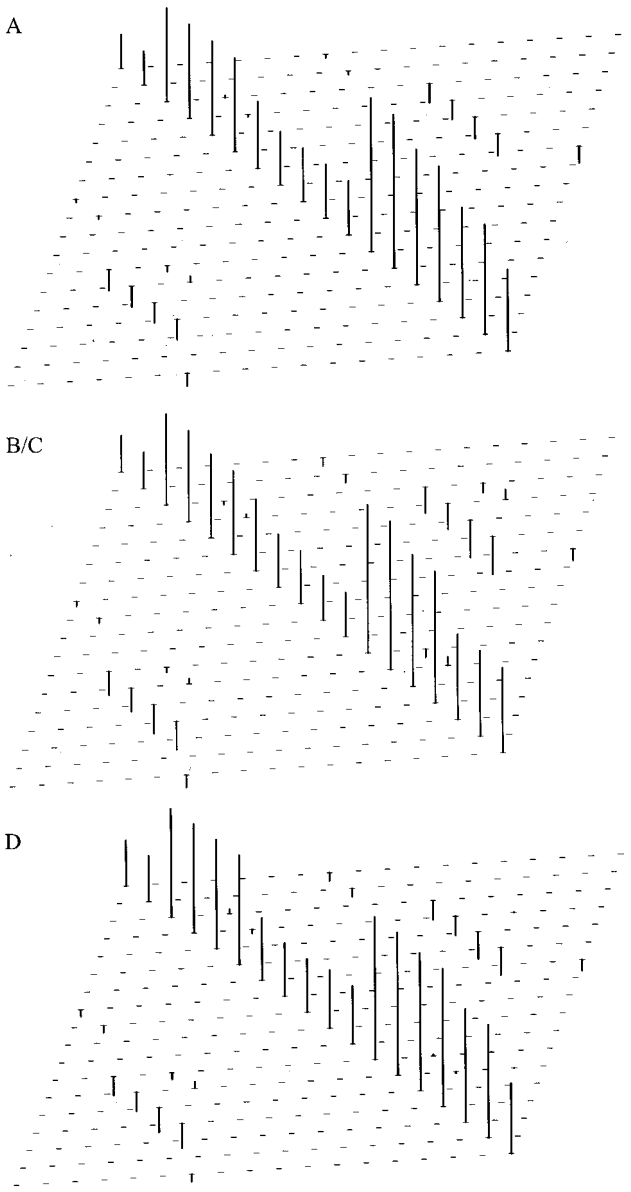

Fig. 4. Graphical representation of the sensitivity matrices for each configuration when the object is a fluorescent volume.

F. Response to a Volume Object

Often microscope specimens consists of thick volumes of fluorescently labeled material, where fluorescence emission occurs throughout the illumination cone. In this case, the specimen could be reasonably approximated by a fluorescent volume that is infinite in extent. The sensitivity of the WFS can be calculated by integration of S_{ik} with respect to u. In other words,

$$S_{Vol,ik} = \int_{-\infty}^{\infty} S_{ik}(u) \mathrm{d}u, \tag{31}$$

where S_{ik} is any of the sensitivities defined above. The sensitivity matrix $\mathbf{S}$ is constructed from the elements S_{ik}. It was shown in Ref. 7 that for the basic WFS, most of the elements of the sensitivity matrix were zero. For each of the WFS configurations A–D, it can again be shown that the sensitivity S_{ik} is identically zero unless both of the following two conditions are satisfied:

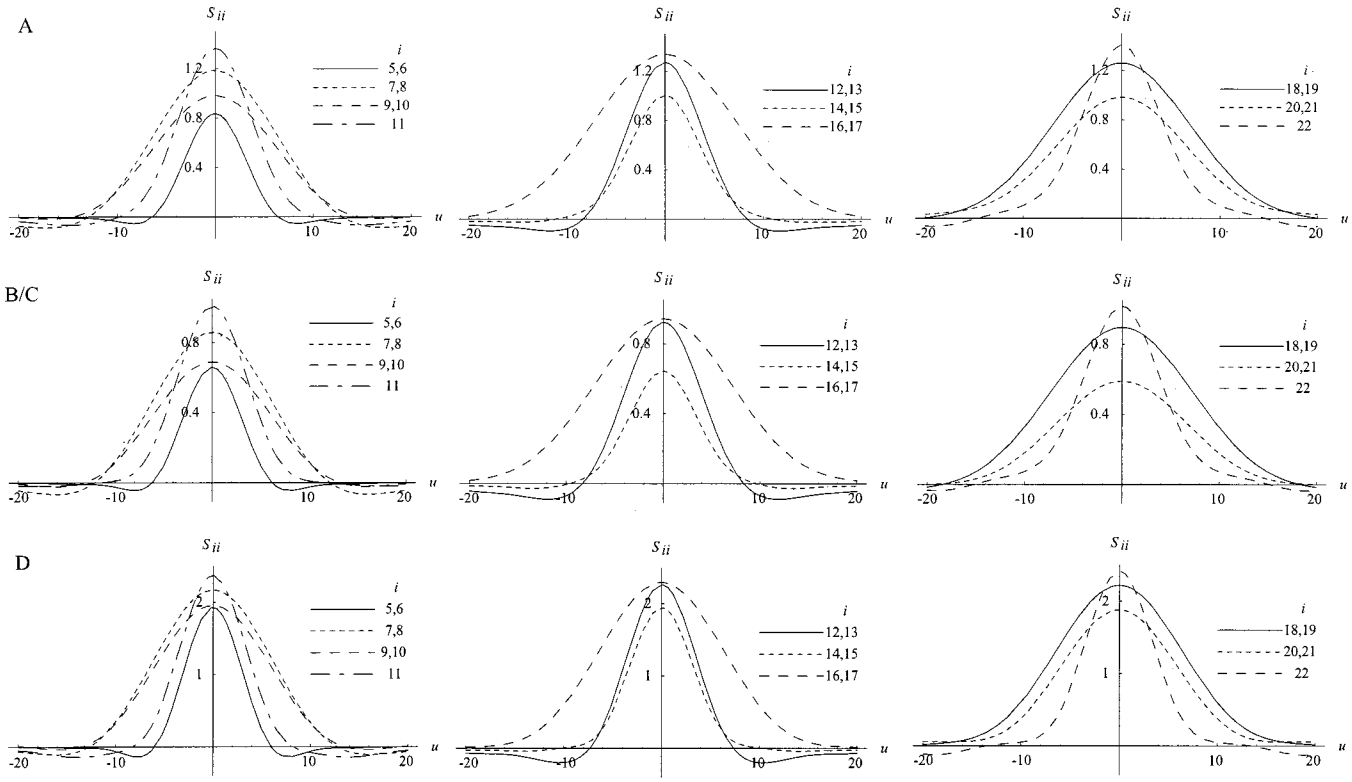

Fig. 5. Axial response to a defocused fluorescent plane for each wave-front sensor configuration. For configuration A, $\nu_p = \pi$ and $b = 0.5$. For configuration B/C, $\nu_p = \pi$ and $b = 0.5$. For configuration D, $b = 0.55$.

1. The azimuthal orders of Z_i and Z_k have the same sign, corresponding to both polynomials containing either a sine term or a cosine term.
2. The azimuthal order m_k of the input mode is an odd multiple of the azimuthal order m_i of the bias mode.

For the sake of brevity, we do not present the proof of this here. Figure 4 shows graphical representations of the sensitivity matrices for configurations A, B/C, and D when the object is an infinite fluorescent volume. Each row represents a sensor designed to detect mode i, and each column represents the input mode k. Values of i and k range from 5 (top left) to 22 (bottom right). Defocus ($i = 4$) cannot be detected when the object is a fluorescent volume. As expected, we see that the sensitivity matrices are sparse with very few off-diagonal elements. We also note that the diagonal values are larger than the off-diagonal values, indicating that each sensor responds predominantly to the mode for which it was designed.

G. Axial Selectivity of the Sensor

The pinhole included in the optical path of a confocal microscope permits only the reflected or the fluorescent light that emanates from outside the focal region to impinge on the detector. This forms the basis of its three-dimensional imaging capabilities. For a WFS to function effectively in an adaptive confocal microscope, it must also demonstrate axial selectivity or become swamped by out-of-focus light, leading to a severely degraded signal-to-noise ratio. The WFS described in this paper incorporates detector pinholes that, like those in a confocal microscope, admit light only from the focal region. The axial selectivity of each sensor can be examined by calculating the sensitivity as a function of the axial displacement of the fluorescent plane u.

Figure 5 shows the axial response for each sensor mode to input Zernike modes 5–22 in configurations A, B/C, and D. In each case the sensors are most responsive to the light emanating from the region of the focus. The full width at half-maximum (FWHM) of the confocal microscope's intensity axial response for a pinhole size $\nu_p = \pi$ is approximately equal to 10. By comparison, some sensor axial responses have narrower FWHMs, and none has a FWHM more than twice that of the confocal response.

3. DISCUSSION AND CONCLUSIONS

We have described how the modal WFS may be implemented in an adaptive confocal fluorescence microscope system in three different biasing configurations. In these configurations the bias aberrations can be added in the illumination path, the emission path, or both simultaneously. Configuration A, where the bias aberration is introduced into both paths, models a system in which the same adaptive element is used for both aberration biasing and aberration correction. Configurations B and C, where the bias aberration is introduced in only the illumination path or the emission path respectively, are appropriate for systems in which the bias aberrations are introduced by an element different from that used for the wave-front correction. Configuration C is particularly useful when a spatially multiplexed aberration-biasing element is employed.[7,8] In this case, a fixed diffractive binary element is placed in the fluorescence emission path

Table 1. Zernike Circle Polynomials

i	n	m	$Z_i(r, \theta)$	Aberration Term
1	0	0	1	piston
2	1	1	$2r\cos(\theta)$	tip
3	1	−1	$2r\sin(\theta)$	tilt
4	2	0	$\sqrt{3}(2r^2 - 1)$	defocus
5	2	2	$2\sqrt{3}r^2\cos(2\theta)$	astigmatism
6	2	−2	$2\sqrt{3}r^2\sin(2\theta)$	astigmatism
7	3	1	$2\sqrt{2}(3r^3 - 2r)\cos(\theta)$	coma
8	3	−1	$2\sqrt{2}(3r^3 - 2r)\sin(\theta)$	coma
9	3	3	$2\sqrt{2}r^3\cos(3\theta)$	trefoil
10	3	−3	$2\sqrt{2}r^3\sin(3\theta)$	trefoil
11	4	0	$\sqrt{5}(6r^4 - 6r^2 + 1)$	spherical (1st)
12	4	2	$\sqrt{10}(4r^4 - 3r^2)\cos(2\theta)$	astigmatism (2nd)
13	4	−2	$\sqrt{10}(4r^4 - 3r^2)\sin(2\theta)$	astigmatism (2nd)
14	4	4	$\sqrt{10}r^4\cos(4\theta)$	
15	4	−4	$\sqrt{10}r^4\sin(4\theta)$	
16	5	1	$2\sqrt{3}(10r^5 - 12r^3 + 3r)\cos(\theta)$	coma (2nd)
17	5	−1	$2\sqrt{3}(10r^5 - 12r^3 + 3r)\sin(\theta)$	coma (2nd)
18	5	3	$2\sqrt{3}(5r^5 - 4r^3)\cos(3\theta)$	trefoil (2nd)
19	5	−3	$2\sqrt{3}(5r^5 - 4r^3)\sin(3\theta)$	trefoil (2nd)
20	5	5	$2\sqrt{3}r^5\cos(5\theta)$	
21	5	−5	$2\sqrt{3}r^5\sin(5\theta)$	
22	6	0	$\sqrt{7}(20r^6 - 30r^4 + 12r^2 - 1)$	spherical (2nd)

and creates an array of spots containing the appropriate aberration biases for the simultaneous measurement of several modes. We have also described a fourth configuration that would be suitable for a two-photon fluorescence microscope in which the bias is introduced only in the illumination path. This can be implemented with a single adaptive element.[9] For each configuration it was shown that the sensor can measure the Zernike components of an aberrated wave front with limited cross sensitivity between modes; this is ideal in confocal and two-photon microscopy, where induced aberrations are typically dominated by a small number of lower-order modes. Furthermore, the sensor demonstrates axial selectivity, responding only to wave fronts emanating from the focal region. This is of obvious benefit in a confocal microscope, where axial sectioning is of the primary importance. In conjunction with an appropriate wave-front-correction element, this WFS would form an integral part of an adaptive confocal microscope.

In this paper we have used a fixed pinhole size and bias amplitudes chosen to give the maximum sensitivity to a planar fluorescent object lying in the focal plane. However, we could equally apply other criteria for calculation of these parameters. For example, we note that in Fig. 4, the on-diagonal sensitivities for certain detector modes are significantly lower than for others; e.g., the sensitivity S_{ii} for first-order astigmatism ($i = 5$ or 6) is approximately 2.5 times smaller than that for first-order coma ($i = 6$ or 7) in configuration B/C. Moreover, in Fig. 5 we see that the axial-sensitivity FWHM for first-order astigmatism is roughly half that for first-order coma. In such cases it is generally possible to increase sensitivity and simultaneously increase the FWHM (with loss of axial selectivity) of certain modes by alternative choice of pinhole size and bias. Further improvement in sensor performance could be produced by combining signals from detectors with different parameter values or even from a combination of circular and annular detectors. By this method, it is possible to reduce the effects of cross sensitivity between modes.

The presence of the linear region in the response graphs of Fig. 3 means that the WFS would be particularly useful in a closed-loop adaptive system in which a correction element, such as a deformable mirror, adaptively corrects dynamic aberrations. The sensitivity of the WFS is dependent on the fluorescence emission from the object. Hence it could be beneficial to normalize the signal by the total fluorescence intensity when the specimen is highly structured, with dark and bright areas. However, the above results suggest another possibility: In addition to the usual primary fluorescent marker, we could introduce nonspecific secondary fluorescent material into the specimen (for example, fluorescent dye or beads that do not selectively mark specific parts of the object) and use the light produced from that fluorophore to measure the aberrations. Furthermore, if this additional fluorophore emits light at a wavelength different from that of the specific fluorescent marker, then it is a simple matter to separate the imaging light from the sensing light by use of a dichroic beam splitter or filter and thus maximize the light efficiency of the microscope. Further improvements could arise if, in addition, the secondary fluorophore could be excited by a wavelength light source different from the primary fluorophore.

APPENDIX A

Table 1 lists the Zernike circle polynomials used in this paper along with their common names. The polynomials can be described by the single index i or the dual index (n, m) where n and m correspond to the radial and azimuthal orders, respectively.

APPENDIX B

The convolution operator is defined in Cartesian coordinates as

$$A(x, y) * B(x, y) = \int_{-\infty}^{\infty}\int_{-\infty}^{\infty} A(x', y') \times B(x - x', y - y')\mathrm{d}x'\mathrm{d}y'. \quad (32)$$

The correlation operator is defined in Cartesian coordinates as

$$A(x, y) \otimes B(x, y) = \int_{-\infty}^{\infty}\int_{-\infty}^{\infty} A(x', y') \times B(x' - x, y' - y)\mathrm{d}x'\mathrm{d}y'. \quad (33)$$

Note added in proof: As reported elsewhere[12] this WFS has been successfully incorporated into an adaptive confocal fluorescence microscope where the WFS was implemented in configuration A by using a deformable membrane mirror as both the biasing and the correction element.

Corresponding author Martin J. Booth can be reached by e-mail at Martin.Booth@eng.ox.ac.uk.

REFERENCES

1. T. Wilson and C. J. R. Sheppard, *Theory and Practice of Scanning Optical Microscopy* (Academic, London, 1984).
2. T. Wilson, ed., *Confocal Microscopy* (Academic, London, 1990).
3. W. Denk, J. H. Strickler, and W. W. Webb, "Two-photon laser scanning confocal microscopy," Science **248**, 73–76 (1990).
4. M. J. Booth, M. A. A. Neil, and T. Wilson, "Aberration correction for confocal imaging in refractive index mismatched media," J. Microsc. **192**, 90–98 (1998).
5. J. W. Hardy, *Adaptive Optics for Astronomical Telescopes* (Oxford U. Press, Oxford, UK, 1998).
6. R. K. Tyson, *Principles of Adaptive Optics* (Academic, London, 1991).
7. M. A. A. Neil, M. J. Booth, and T. Wilson, "New modal wavefront sensor: a theoretical analysis," J. Opt. Soc. Am. A **17**, 1098–1107 (2000).
8. M. A. A. Neil, M. J. Booth, and T. Wilson, "Closed-loop aberration correction using a modal Zernike wave-front sensor," Opt. Lett. **25**, 1083–1085 (2000).
9. M. A. A. Neil, R. Juskaitis, M. J. Booth, T. Wilson, T. Tanaka, and S. Kawata, "Adaptive aberration correction in a two-photon microscope," J. Microsc. **200**, 105–108 (2000).
10. J. W. Goodman, *Introduction to Fourier Optics* (McGraw-Hill, London, 1996).
11. Min Gu, *Principles of Three-Dimensional Imaging in Confocal Microscopes* (World Scientific, Singapore, 1996).
12. M. J. Booth, M. A. A. Neil, R. Juskaitis, and T. Wilson, "Adaptive aberration correction in a confocal microscope," Proc. Natl. Acad. Sci. USA **99**, 5788–5792 (2002).